Noise Reduction Using Spatial-Angular Compounding for Elastography

Udomchai Techavipoo, *Student Member, IEEE*, Quan Chen, *Student Member, IEEE*, Tomy Varghese, *Senior Member, IEEE*, James A. Zagzebski, *Associate Member, IEEE*, and Ernest L. Madsen

***Abstract*—Ultrasound elastography has developed into an imaging modality suitable for detection and diagnosis of cancers in the breast, prostate, and thyroid and for monitoring ablative therapies in the liver, kidneys, and other sites. In this article, a new approach is described that enables the reduction of noise artifacts in elastography without a significant reduction in either the contrast or spatial resolution. The technique uses angular-weighted compounding of local angular strains estimated from echo signals scanned at different insonification angles. Strain estimated along angular insonification directions can be separated into strain tensor components along the axial (direction of compression) and lateral directions. The mechanical stimulus is applied only along one direction. Angular-weighting factors are derived from the relationship between the axial and lateral strains under the assumption of tissue incompressibility. Experimental results using a uniformly elastic, tissue-mimicking phantom demonstrate the improvement in the signal-to-noise ratio obtained with angular-weighted compounding. Variation in the signal-to-noise ratio obtained using different angular increments also is investigated. Elastograms obtained from an inclusion phantom also demonstrate the improvement in contrast detail resolution obtained using spatial-angular compounding.**

I. Introduction

Over the past decade, imaging of tissue stiffness has gained interest for diagnosis of disease [1]–[16]. The term stiffness refers to local strain values in response to a uniaxial stress; the lower the local strain, the stiffer the material. Pathological changes in tissue generally are accompanied by changes in tissue elastic moduli. For example, scirrhous carcinoma appears frequently as a hard nodule, and liver tissue with cirrhosis is known to be stiffer than normal liver tissue [17]. These pathological changes may not significantly alter the tissue's echogenic properties, thus making it difficult to detect them with conventional ultrasound. Elastography is an imaging technique in which local strains are estimated by computing the gradient of axial shifts in echo arrival times after a quasistatic tissue compression. The axial shifts are computed using cross-correlation analysis, applying overlapping windows to the echo data to improve resolution. However, a high degree of overlap introduces distortions in strain estimates due to correlation artifacts [2], [3].

Investigators have tried to minimize correlation artifacts by using algorithms such as temporal stretching [18], [19], adaptive stretching [20], multicompression averaging [21], or wavelet denoising [22]. Temporal stretching is an effective algorithm for this task. However, it requires a priori knowledge of the applied compression, and it works most effectively when imaging homogenous and uniformly elastic media. It stretches the postcompression signals with a known compression factor before estimating axial strains. Wavelet denoising smoothes the displacement estimates in the wavelet domain without losing edge information. Multicompression averaging reduces noise by averaging elastograms generated using successive small compressions. In addition, most of these algorithms can be used in conjunction with the other for artifact reduction in elastography.

For conventional ultrasound imaging, speckle noise may be reduced significantly by spatial compounding [23]–[29]. This method involves averaging ultrasound images around the same region-of-interest but from different views. Assuming that N independent ultrasound images are averaged, the signal-to-noise ratio (SNR; the mean gray scale level divided by its standard deviation) will increase by a factor of $\sqrt{N}$ [23]. This approach has been used and implemented on commercial ultrasound scanners by steering the beam from a linear or curvilinear array transducer [29]. Tanter *et al.* [26] also have demonstrated the use of ultrafast compounding for applications in transient elastography.

In this paper, we investigate the use of spatial-angular compounding to reduce noise artifacts in elastograms, by spatially compounding angular elastograms acquired at different insonification angles. A unidirectional, quasistatic compression force is applied, and pre- and postcompression radio-frequency (RF) echo signals are acquired at different insonification angles. The method is tested by translating a phased-array ultrasound transducer over the sample. Angular elastograms estimated at different insonification angles generated using these data are appropriately weighted (depending on the insonification angle), then averaged to produce a spatially compounded elastogram. We present results obtained using uniformly elastic and single inclusion phantoms that demonstrate the improvement in the elastogram's quality parameters such as the signal-to-noise ratio (SNR_e).

Manuscript received May 19, 2003; accepted December 3, 2003. This research was supported in part by start-up funds provided to Dr. Varghese from the Department of Medical Physics, Medical School and Graduate School at the University of Wisconsin, Madison, and NCI grant R21 EB002722.

The authors are with the University of Wisconsin-Madison, Madison, WI 53706 (e-mail: tvarghese@wisc.edu).

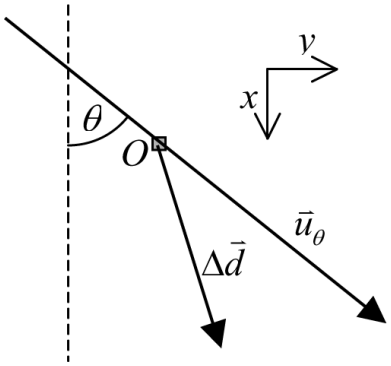

Fig. 1. The diagram illustrates the computation of the axial and lateral component of the displacement vector from the angular displacement vector. The ultrasound beam u_θ, and the vector Δd, which denotes the difference between the actual displacement vectors associated with two consecutive local displacements observed along u_θ, are shown. These local displacements are located such that point O is at the center and displacements are along the ultrasound beam u_θ direction.

II. Theory

The apparent strain computed at any fixed pixel location in an ultrasound image depends on the direction or angle along which it was measured. In this section, we present a relationship between local strain estimated using an ultrasound beam u_θ at insonification angle θ with respect to the compression axis, and the corresponding component strains along the x (direction of compression; the axial direction for conventional elastography) and y (perpendicular to the direction of compression, and in the image plane) directions, respectively. In elastography, local strains are estimated by computing the gradient of the displacement estimates. These gradients may be approximated by differences between local displacements of consecutive segments of an echo signal divided by the local separation of these segments or by using an algorithm to estimate the slopes of multiple local displacement estimates in the spatial domain using least squares to estimate strain [30]. An illustration of this concept is shown in Fig. 1, in which we assume that local strains at point O were detected by the ultrasound beam u_θ. The local strain was estimated from the displacement of two consecutive echo signal segments, as previously described. These segments are along the same ultrasound beam u_θ, and their origins are located such that point O is at their center. Let $\vec{d}_1$ and $\vec{d}_2$ be the actual displacement vectors associated with these observed or estimated displacements. The difference between the observed displacements along ultrasound beam u_θ can be written as:

$$\Delta d_\theta = \left(\vec{d}_2 - \vec{d}_1\right) \cdot \vec{a}_\theta = \Delta\vec{d} \cdot \vec{a}_\theta, \tag{1}$$

where $\vec{a}_\theta$ is a unit vector parallel to the ultrasound beam u_θ, and $\Delta\vec{d}$ is the difference between the actual displacement vectors. These vectors could be decomposed into components in the x and y directions; (1) then can be written as:

$$\Delta d_\theta = \Delta d_x \cos\theta + \Delta d_y \sin\theta, \tag{2}$$

where Δd_x and Δd_y are the displacement components along the x and y direction of $\Delta\vec{d}$, and $\cos\theta$ and $\sin\theta$ are the x and y components of the unit vector $\vec{a}_\theta$, respectively. Let Δz_θ denote the distance between the locations of these displacements along the θ direction. Therefore, the strain at point O observed along the θ direction can be written as:

$$e_\theta = \left(\Delta d_x \cos\theta + \Delta d_y \sin\theta\right) / \Delta z_\theta. \tag{3}$$

The distance Δz_θ can be decomposed into $\Delta z_x = \Delta z_\theta \cos\theta$ and $\Delta z_y = \Delta z_\theta \sin\theta$ in the x and y directions, respectively. Using these relationships, (3) can be rewritten as:

$$e_\theta = e_x \cos^2\theta + e_y \sin^2\theta, \tag{4}$$

where $e_x = \Delta d_x / \Delta z_x$ and $e_y = \Delta d_y / \Delta z_y$ are the strain components in the x and y directions, respectively. Assuming uniaxial stress conditions, in which the Poisson' ratio can be approximated as the negative ratio of the strain in the lateral (y) direction to the axial (x) direction (i.e., $\nu = -e_y/e_x$), the strain components along the x and y directions can be written as follows:

$$\begin{aligned} e_x &= e_\theta / \left(\cos^2\theta - \nu \sin^2\theta\right), \\ e_y &= e_\theta / \left(\sin^2\theta - 1/\nu \cos^2\theta\right). \end{aligned} \tag{5}$$

Note from (5) that the strain components in the x and y direction (e_x and e_y) are related to the angular strain e_θ by the weighting factors, defined as follows:

$$\begin{aligned} w_x(\nu,\theta) &= 1 / \left(\cos^2\theta - \nu \sin^2\theta\right), \\ w_y(\nu,\theta) &= 1 / \left(\sin^2\theta - 1/\nu \cos^2\theta\right). \end{aligned} \tag{6}$$

The weighting factor, therefore, depends on the Poisson's ratio and the ultrasound insonification angle. The strain components in the x and y directions thus can be written as follows:

$$\begin{aligned} e_x &= e_\theta w_x(\nu,\theta), \\ e_y &= e_\theta w_y(\nu,\theta). \end{aligned} \tag{7}$$

From (7), if we assume that the tissue is incompressible, where $\nu \cong 0.495$, estimates of the axial and lateral strain components can be obtained from the angular-strain estimate.

III. Materials and Methods

Elastographic imaging performance using angular-spatial compounding was assessed using both uniformly elastic and single-inclusion phantoms of size $10 \times 10 \times 10$ cm manufactured in our laboratory [31]. The inclusion phantom contains a 1-cm diameter cylindrical inclusion with a strain contrast of 2.4 (expected modulus contrast of 3.8) with the background. The uniformly elastic phantom was used to investigate improvements in elastographic

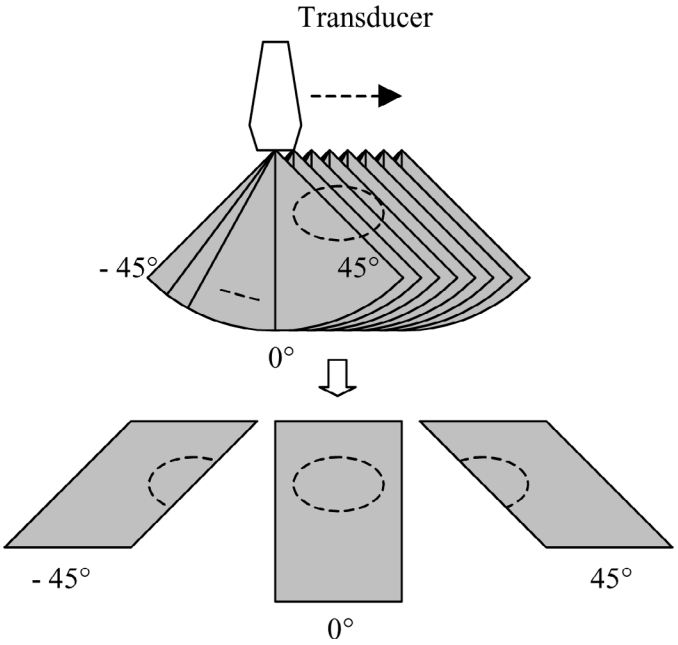

Fig. 2. RF data sets in sector format (top) acquired at each lateral position. These scans were rearranged into angled RF data sets (bottom) by grouping A-lines acquired for the same beam angle.

SNR_e obtained using spatial compounding, and the single-inclusion phantom was applied to study if any marked reduction in the spatial definition of the inclusion boundary occurs with spatial compounding. Both phantoms were scanned using an Aloka SSD 2000 (Aloka Inc., Tokyo, Japan) real-time scanner using a 3.5 MHz phased-array transducer with an approximately 60% bandwidth. To simulate the effects of compound data acquisition of RF echo signals, the phased array transducer was linearly translated over the phantom sample using a precision linear stage so each location in the sample was scanned from multiple angles as shown in Fig. 2.

A compression plate with a rectangular slot fitted with the transducer aperture was mounted to the transducer. The compression plate is larger than the phantom surface, providing uniform compression of the phantom. Echo signals were acquired from the phantom before and after a compression of 1% of the phantom height. The compression was applied in the axial direction of the central beam line forming the image. The combined transducer-plate fixture was laterally translated (parallel to and on the imaging or scanning plane) over a distance of 40 mm, and signals were recorded at 1/6-mm increments. Thus, over the 40-mm lateral distance, 240 pre- and postcompression RF data sets were acquired. A data set consists of 120 A-lines arranged over a 90° sector. The ultrasound (US) RF signals were digitized using a 12-bit data acquisition board (Gage Inc., Montreal, Quebec, Canada) at a sampling rate of 50 MHz. During off-line analysis, the data sets were rearranged so that the A-lines along the same angle from all the sector images were grouped together to form RF frames at that angle. This is illustrated in Fig. 2, in which the distance between the A-lines in the regrouped data was 1/6 mm. Acquisition of the data in this manner provided RF frames over an angular range up to ±45°, with a minimum angular increment of 0.75°.

Each of these regrouped RF frames was analyzed separately to generate an elastogram at the specified angle, referred to as an angular elastogram. Angular elastograms were computed using the following procedure. A cross-correlation algorithm using a window size of 3 mm and 75% overlap of consecutive windows was used to generate displacement estimates. A 5-point, one-dimensional (1-D) median filter then was applied to eliminate the outliers in the displacement estimates. A 3-point, least squares strain estimator [30] was used to generate local strain estimates. Angular elastograms were filtered using a 5×5 median filter to suppress strain outliers.

Spatial compounding for elastography was performed in two stages. Each angular elastogram was appropriately weighted, following which spatial averaging of the weighted and registered angular elastograms was performed to obtain the compounded elastogram. Prior to compounding, spatial registration was performed on the angular elastograms using bilinear interpolation [32], [33]. Two factors, namely the angular increment used and the number of angular elastograms averaged have a significant impact on the enhancement of the elastogram quality. Compound elastograms were obtained by weighted averaging over different angular increments ($\Delta\theta$) and numbers of angular elastograms (N). The strain estimate computed for each image or pixel location is given by:

$$C(\Delta\theta, N) = \frac{1}{N} \sum_{i=-n}^{n} w_x(\nu, i\Delta\theta) A(i\Delta\theta), \tag{8}$$

where $C(\Delta\theta, N)$ represents a compound elastogram. N is the number of angular elastograms used in compounding, which equals $2n + 1$, where n is the number of angular elastograms in either the positive or negative angular direction. $A(\theta)$ and $w_x(\nu, \theta)$ are the angular elastogram and the weighting factor for axial strains at angle θ.

We considered only cases using compounding of symmetrical positive and negative angles as shown in the summation index of (8). Therefore, the total number of angular elastograms used in compounding is $2n + 1$ as described before. In our notation, a compound elastogram will be identified by its maximum angle, $n\Delta\theta$, with $\Delta\theta$ values of 0.75°, 1.5°, 3.75°, and 7.5° being applied (the minimum $\Delta\theta$ value being 0.75° for our phased-array transducer).

The values of the mean, variance, and SNR_e were analyzed for angular and compound elastograms. We selected only the common spatial region within the RF echo data set (i.e., the area within which all angular elastograms intersect) to obtain these statistical estimates. Values both with and without the use of the weighting factors were computed. The elastographic SNR [4], [34] is defined as:

$$\mathrm{SNR}_e = \mu/\sigma, \tag{9}$$

where μ and σ are the sample mean and standard deviation of the strains over pixels in the common region.

IV. Results

We initially present the elastograms or strain images obtained at different angular insonifications and discuss the strain imaging performance over the range of angles used in this study. We then present results obtained by combining the angular elastograms to generate compound elastograms.

A. Angular Elastograms

Fig. 3 presents plots of the mean and variance of strains in elastograms obtained at different insonification angles. Mean and variance values are presented with and without the appropriate angular weighting to obtain the axial-strain estimates. The dotted lines around the strain and variance estimates represent the standard deviation of the mean estimates obtained over eight independent experiments. Without angular weighting, the quantity plotted is the observed strain at each insonification angle (e_θ), which varies with angle. After weighting is applied, we obtain the strain component along the x or axial direction (e_x), independent of the insonification angle.

Compounding is meaningful only for estimates in which the expected or mean value is obtained after the averaging process. Therefore, for the angular-compounding results presented in this paper, angular weighting is used prior to compounding. In Fig. 3(a), we observe an increased uniformity among the strain estimates obtained at different angles when appropriate angular weights are assigned to the angular-strain images. However, the strain estimates at larger insonification angles are still lower than the expected value. We believe that this is caused by increased errors at those angles due to decorrelation of the pre- and postcompression RF A-lines. An increased variance also is observed at the larger angles, as shown in Fig. 3(b). The method used for angular weighting magnifies the variance of axial strains, especially for large angles. In addition, note that the curve is not symmetric with the 0° insonification angle. We believe that this is due to asymmetry among the beams transmitted by the phased-array transducer, possibly due to different sensitivities of the transducer elements for different insonification angles.

Examples of angular elastograms before weighting, obtained from a uniform phantom, are shown in Fig. 4, for angles of 0°, 12°, and 18.75°. As expected, we observed more noise in the strain images at larger angles. Elastograms obtained when the beam angle relative to the direction of compression is large suffer from significant decorrelation of the pre- and postcompression RF echo signals, especially at increased depths. This is explained by the geometric location of the A-lines before and after compression. For example, consider a θ-angled, A-line segment, starting at a point O in the phantom. After compression, the scatterers in the path of the precompression A-line within the phantom rotate around point O, but the postcompression A-line is maintained at the same θ angle. Therefore, deeper segments of RF A-lines at large beam angles decorrelate more rapidly, resulting in increasing the noise in the strain estimates, as observed in Figs. 4(b) and (c). We also observe a reduction in brightness at larger angles, implying that the strains measured at larger angles are lower than those measured at small angles. However, appropriate angular weighting will compensate for the effects illustrated in Fig. 4.

The $\mathrm{SNR_e}$ in the angular elastograms obtained at different insonification angles is illustrated in Fig. 5. The angular weights used do not impact the $\mathrm{SNR_e}$ of individual elastograms because the weight factor is applied to both the mean and standard deviation, thus canceling its effect on the $\mathrm{SNR_e}$. The impact of global temporal stretching is shown in Fig. 5(b), which is contrasted with no temporal stretching in Fig. 5(a). Temporal stretching improves the correlation between the pre- and postcompression RF signals, thereby reducing the noise in strain estimates [18]–[21] with a subsequent increase in the $\mathrm{SNR_e}$. The use of temporal stretching provides a larger range of insonification angles over which the axial component of the strain estimates can be effectively compounded. Fig. 5(a) shows that, although compounding the angular elastograms over ±15° would provide significant improvements in the $\mathrm{SNR_e}$ without temporal stretching, compounding can be performed over ±22° with temporal stretching.

B. Compounded Elastograms

The dependence of the mean strain and the strain variance on the extent of compounding is presented in Fig. 6. Results are shown for different angular increments and are plotted as a function of maximum angle used to obtain the compounded elastogram. The mean and variance plots shown in Fig. 6 were obtained without temporal stretching. The error bars of the mean strain and variance plots denote the standard deviation of the mean estimates over eight independent data sets, and are presented only for selected data points to improve the clarity of the figure. Results are shown only with angular weighting from this point forward. Note that in Fig. 6(a), with appropriate angular weighting, the mean strain estimates are nearly constant at different maximum angles over which compounding is performed. The variance of the strain estimate reduces significantly with increased compounding, as shown in Fig. 6(b).

Comparing the strain variance versus maximum angle for different angular increments in Fig. 6(b), the curves are almost identical, except for the 7.5° increment, which is noticeably higher than the others. The strain variance for the 7.5° angular increment does not drop as low as that for the other increments due to the smaller number of averaged elastograms at any maximum angle. The strain-estimation variance for the 7.5° angular increment actually increases when the maximum angle used for compounding exceeds 15° due to contributions from the increased errors at large insonification angles. With only a few elastograms contributing to the compound elastogram, errors at large angles are more heavily weighted.

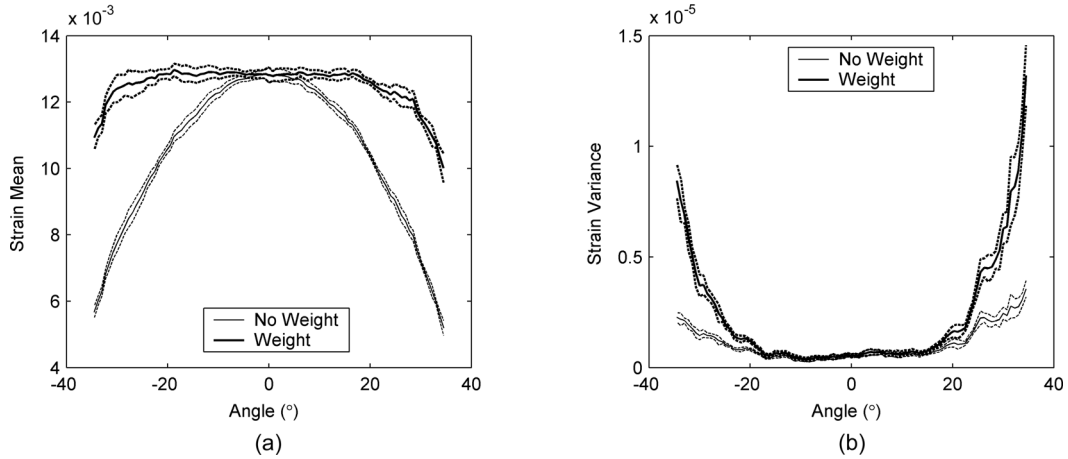

Fig. 3. Mean strain (a) and strain variance (b) versus insonification angle. Strain estimates obtained with weighting (thick solid line) and without weighting (light solid line) are depicted. The dotted lines denote plus and minus one standard deviation from the mean value across eight independent data sets. Elastograms were obtained without global temporal stretching.

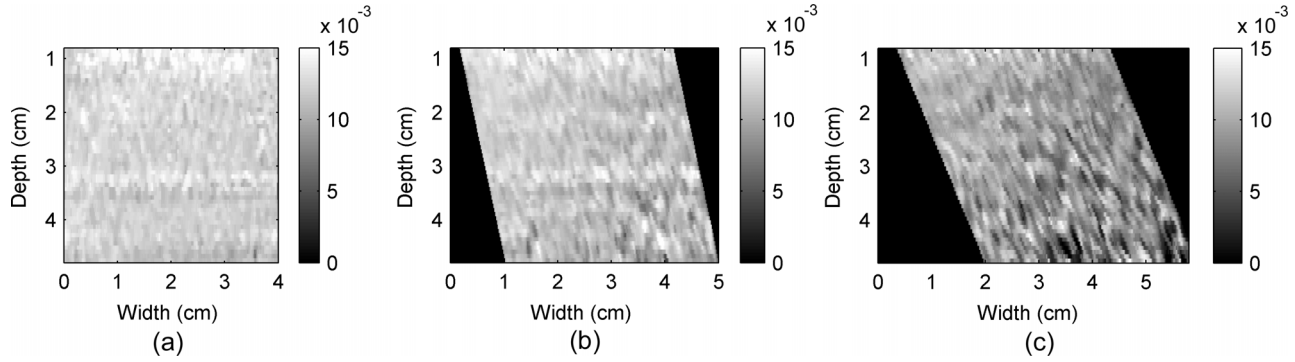

Fig. 4. Angular elastograms obtained at (a) 0°, (b) 12°, and (c) 18.75°angles before weighting and without global temporal stretching. The colorbar denotes strain, where 1% strain is displayed as 0.01.

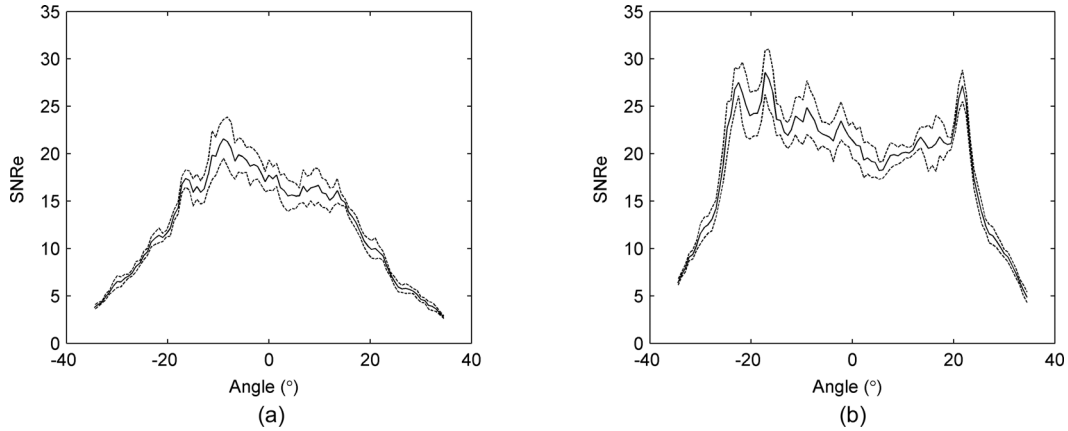

Fig. 5. Elastographic SNR_e for eight independent data sets versus insonification angle (a) without and (b) with global temporal stretching. Note that the angular weighting factor does not affect the SNR_e.

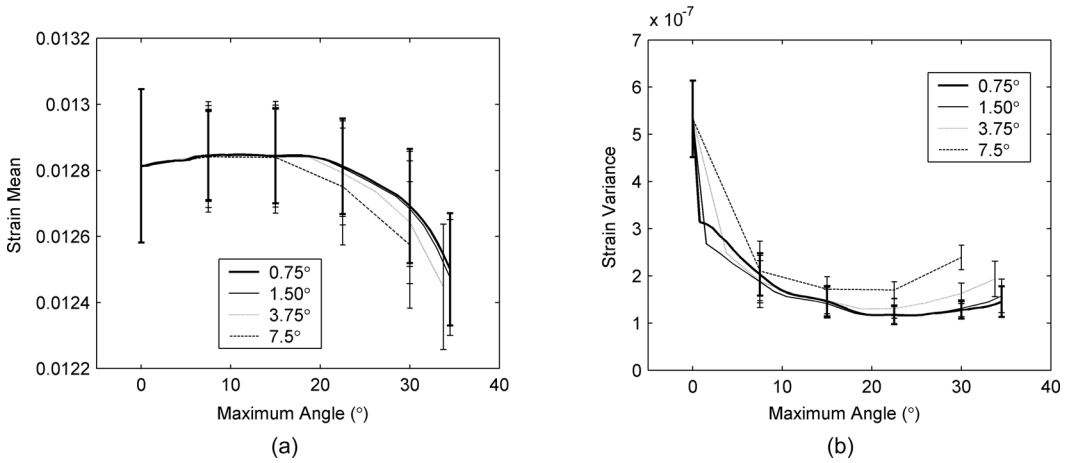

Fig. 6. (a) Mean strain and (b) strain variance of compound elastograms versus the maximum angle over which compounding was performed. Results obtained using 0.75°, 1.50°, 3.75°, and 7.50° angular increments are shown. The angular increment of 0.75° is the smallest angular increment obtained using the phased-array transducer. The error bars denote the standard deviation over eight independent experiments.

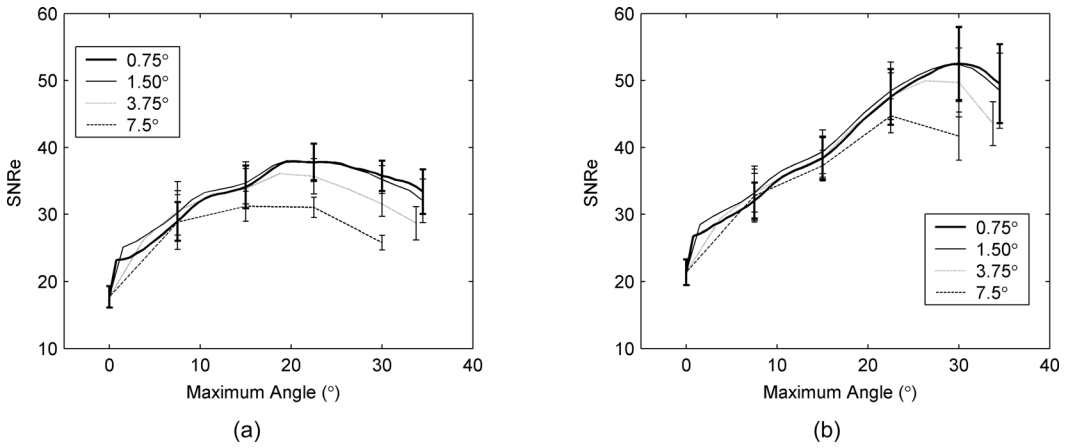

Fig. 7. Mean SNR_e and standard deviation (error bars) of the angular compounded elastograms (a) without and (b) with global temporal stretching, versus the maximum angle over which compounding was performed. Results obtained using 0.75°, 1.50°, 3.75°, and 7.50° angular increments are shown.

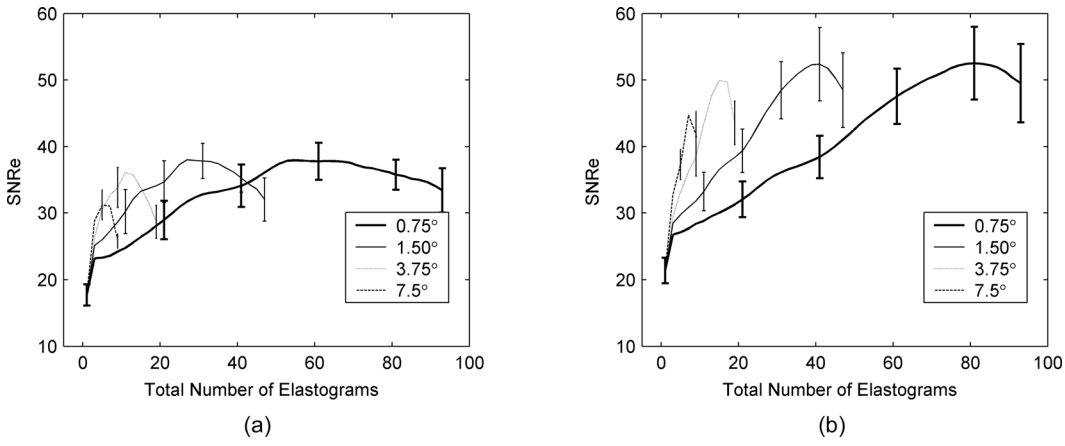

Fig. 8. Mean SNR_e and standard deviation (error bars) of angular compounded elastograms versus total number of elastograms over which compounding was performed. Results obtained using 0.75°, 1.50°, 3.75°, and 7.50° angular increments are shown.

The improvement in the elastographic SNR_e with spatial angular compounding is demonstrated in Figs. 7 and 8. The error bars in Figs. 7 and 8 denote the standard deviation of the SNR_e estimates over the eight independent experiments and, again, are presented for only a small number of data points for clarity. The SNR_e versus maximum compounding angle plots are presented without [Fig. 7(a)] and with [Fig. 7(b)] temporal stretching. Without temporal stretching, the compounded SNR_e increases with angle to about 18.75° (maximum SNR_e value), then it slightly decreases with increased compounding. The SNR_e ranges from about 16 at 0° (no compounding) to about 38 at the 18.75° maximum angle, a factor of 2.4. The SNR_e for the larger angular increment of 7.5° reduces significantly for maximum angles greater than 10° due to the presence of increased noise at larger insonification angles, as mentioned above. Other angular increments provide similar results, although we observe reductions in the SNR_e for maximum angles greater than 18.75° for the 3.75° angular increment. Results obtained with temporal stretching in Fig. 7(b) demonstrate an increase in the SNR_e from about 22 at 0° (no compounding) to about 52 at a maximum angle of 30°, again a factor of about 2.4. The trends observed in the case without temporal stretching [Fig. 7(a)] also are observed in Fig. 7(b), however, at larger maximum angles.

The SNR_e is plotted versus the number of angular elastograms used for compounding in Fig. 8. The importance of having independent and uncorrelated data sets is demonstrated in this plot. In this case the angular increments of 3.75° and 7.5° provide the fastest rise in the SNR_e versus total number curve as the strain estimates used in the compounding process are from echo data that are statistically more independent than those obtained for the smaller angular increments. However, the highest value of the SNR_e obtained for the 7.5° increment is lower than that obtained for the other angular increments due to the fewer number of angular strain data available for compounding. In general, smaller angular increments require a larger number of elastograms to be compounded to obtain similar increases in the SNR_e. For the transducer used in this study, the angular increment of 1.5° provides the best tradeoff in image quality versus acquisition time because fewer angular elastograms need to be averaged to obtain similar increases in the SNR_e. As can be seen in Fig. 8, use of 30 angular elastograms separated by 1.5° increments provides the same SNR_e as 60 angular elastograms separated by 0.75°. The results obtained with temporal stretching in Fig. 8(b) demonstrate a similar trend.

Compound elastograms are shown in Fig. 9, in which an angular increment of 0.75° and maximum angles of 12° and 18.75° were used during spatial angular compounding. These compounded elastograms demonstrate an improvement in SNR_e over that for conventional elastograms, obtained without compounding, as in Fig. 4(a). The first panel [Fig. 9(a)] shows compound elastograms obtained without temporal stretching. The region demarcated by the two dashed lines on the elastogram represents locations for which strain estimates were obtained and averaged for all the insonification angles. The region outside the demarcated zone is made up of fewer numbers of strain estimates. Notice that the demarcated area becomes smaller for larger maximum angles as illustrated in the images on the right side of the panel. The second panel [Fig. 9(b)] shows compound elastograms obtained using temporal stretching. The horizontal bands observed in the elastograms in Figs. 9(a) and (b) are due to artifacts in our phased-array transducer. The third panel [Fig. 9(c)] shows a map of the number of angular estimates used at each strain pixel for compounding. As mentioned above, the region that contains all possible angular estimates is smaller for the larger maximum compounding angle.

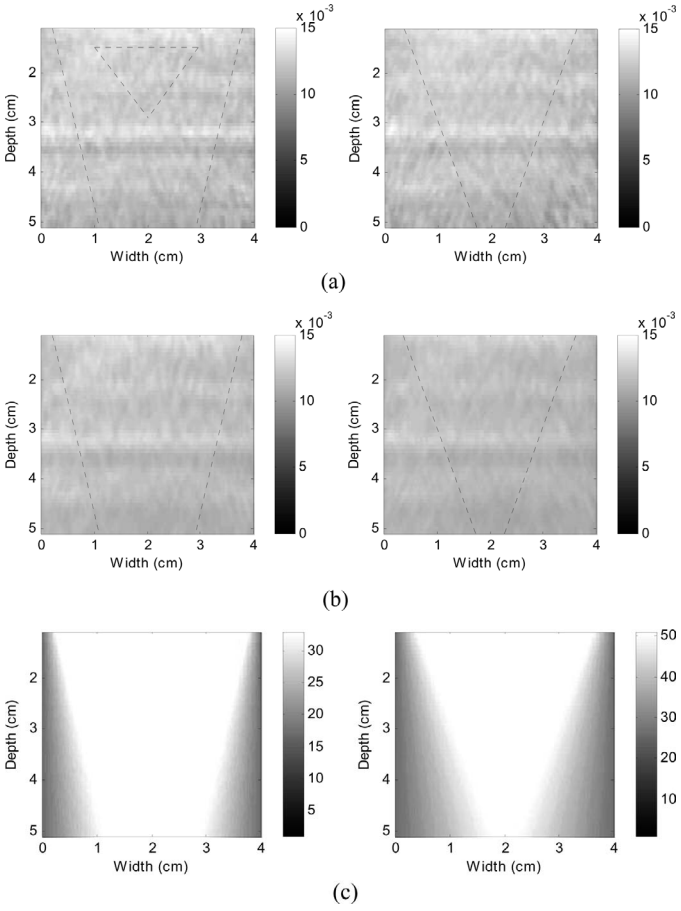

Fig. 9. Compound elastograms obtained (a) without and (b) with global temporal stretching. The number of strain estimates used to obtain each pixel in the elastograms in (a) and (b) are shown in (c). Elastograms were obtained using an angular increment of 0.75° over maximum angles of 12° (left) and 18.75° (right), respectively. Mean and variance of strain estimates were computed over the triangular region shown on the elastogram (left). The region demarcated by the two dashed lines represents locations common to all angular elastograms compounded.

Elastograms obtained from the inclusion phantom are shown in Fig. 10. A comparison of the elastogram in Fig. 10(a) obtained without compounding to the compounded elastograms demonstrates a significant reduction in noise artifacts and subsequent improvement in the detectability of the inclusion using compounding. The im-

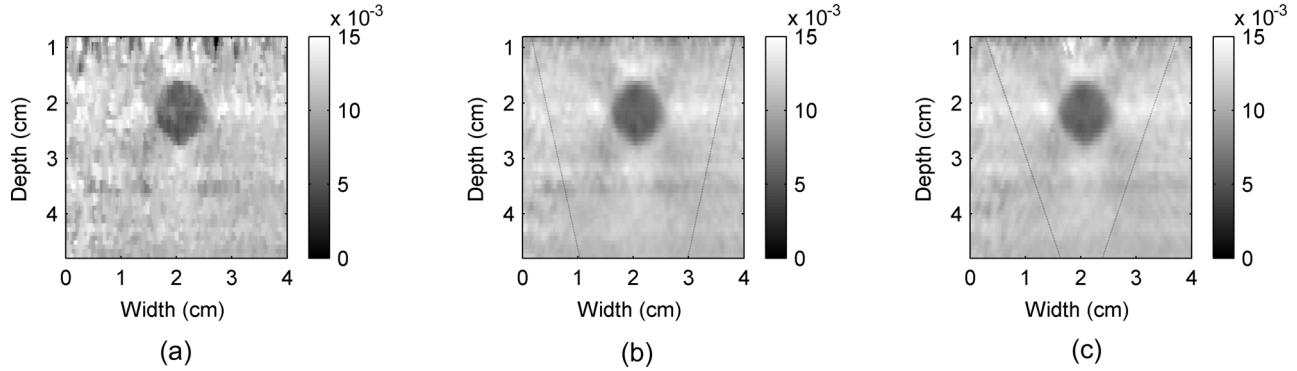

Fig. 10. Elastograms of the inclusion phantom (a) without compounding, (b) compounding with a maximum angle of 12°, and (c) 18.75°, using 0.75° angular increments.

provement in the contrast detail resolution obtained using spatial angular compounding also is seen clearly, where the edges of the inclusion are clearly demarcated and the visualization improves with increased compounding.

V. Discussion

Angular compounding of ultrasound B-mode images is currently performed on a number of commercial clinical scanners to improve ultrasound images by reducing speckle noise artifacts. In this paper, we describe the use of spatial angular compounding in strain elastograms. Angular compounding reduces noise in elastograms, thus improving the $\mathrm{SNR_e}$ as demonstrated in this paper. The improvement in strain images obtained with angular compounding has been demonstrated using both quantitative performance measures and strain elastograms. The improvement in the elastograms is observed by comparing corresponding noncompounded elastogram in Fig. 4(a) with compounded elastograms in Figs. 9(a) and 10. No degradation in the spatial or contrast resolution with compounding is apparent from the elastograms of the single inclusion phantom, shown in Fig. 10.

The importance of angular weighting to obtain only the axial component of the strain is stressed in this paper. Use of appropriate weights shown in (6) converts the observed angular strain e_θ into a quantity (e_x) that is independent of insonification angle so that spatial-angular compounding can be performed. Angular weighting extends the range of insonification angles over which spatial angular compounding can be performed. Global temporal stretching reduces strain estimate noise caused by signal decorrelation between pre- and postcompression RF echo signals. It also increases the range of useful insonification angles over which compounding can be performed. However, we have to point out that temporal stretching is most effective with uniformly elastic and homogenous phantoms or tissues under 1-D motion conditions. The theoretical results presented in this paper also illustrate the ability to generate compounded lateral strain images under the assumption of tissue incompressibility. This assumption is true for most soft tissues and tissue-like materials [37], [38]. However, axial and lateral strains could be estimated from a set of strains measured in different angles without using the incompressibility assumption.

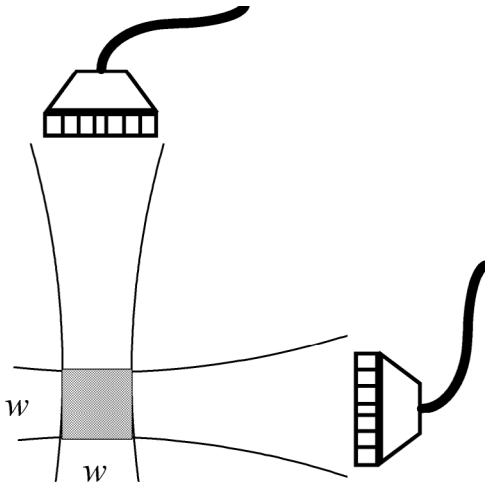

Fig. 11. Schematic of the overlapping region of interest (shaded square) obtained for perpendicular angular insonification.

For most other spatial compounding techniques (e.g., compounding data from adjacent beam lines), the signals have to arise from different spatial locations to be sufficiently decorrelated. In these techniques, the improvement in SNR is at the expense of spatial resolution. In essence, these techniques are similar to applying a low-pass filter to the final image. However, angular compounding compounds signals from the same spatial location. But, because these signals come from different insonification angles, the signals are sufficiently decorrelated [25], [27], [28]. Therefore, it is possible to get $\mathrm{SNR_e}$ improvements using angular compounding without sacrificing spatial resolution. Assuming that the window length used for estimating strain is approximately equal to the beam width (w), then the shaded square box shown in Fig. 11, with dimension of $w \times w$ would be the ROI for the strain estimate. When we insonify the same region at 90° to obtain another strain estimate and compound these estimates, the ROI's overlap, with no loss in spatial resolution, but with significant decorrelation in the RF signals and an improvement in

the SNR_e. Note that the window length used in this paper is 3 mm with 75% overlap in the data segments. It is definitely possible using the 3-mm window length that increased angular insonification would increase the region of interest, leading to a possible loss in the spatial resolution. However, the increased SNR_e obtained with angular compounding allows for a tradeoff, or a subsequent reduction in the window length to offset the sacrifice in the spatial resolution [35]. Previous research using simulation studies place the measured elastographic axial resolution to be on the order of the ultrasonic wavelength [36]. The increased SNR_e obtained with angular compounding could help achieve the spatial resolution described by Righetti *et al.* [36], in which small regions of interest with maximum overlap are best.

The largest increases in the SNR_e are obtained by averaging independent, uncorrelated strain estimates [25]. The effective number of independent estimates depends on two factors: the angular increment and the number of angular elastograms used in compounding. Angular increments of 0.75° to 3.75° provide similar improvements in SNR_e for a fixed maximum angle (see Fig. 7). However, a larger number of spatial averages are required to achieve a given level of SNR_e for the smaller angular increments because of partial correlation of the RF data. Because RF data from a tissue volume viewed with beams separated by a small angular increment are more correlated than those viewed with beams separated by a large increment [25], [27], [28], the correlation between strains estimated from a small angular difference are significantly larger than those estimated from a larger angular difference. The most efficient angular increment for this particular setup appears to be about 3.75°, as indicated in Figs. 7 and 8.

The second factor that affects the SNR_e of compound elastograms is the number of angular elastograms used. Increasing the number of elastograms compounded reduces the strain variance and improves the SNR_e. However, it also requires use of elastograms scanned over larger insonification angles, in which there is increased strain variance, as shown in Fig. 3(b). The maximum angle that can be used in angular compounding for this particular setup should not exceed 18.75° (without temporal stretching), as shown in Fig. 7(a).

Larger angular increments for compounding provide a faster improvement in the SNR_e (see Figs. 7 and 8) and reduce the computational time. However, as previously discussed, a tradeoff exists between the use of larger angular increments and the number of elastograms available for compounding.

VI. Conclusions

The results shown in this paper imply the possibility of obtaining an optimal angular increment for efficient spatial compounding. The use of an optimal angular increment would help to significantly reduce the computational burden and yet obtain the maximum improvements in the SNR_e by a factor of $\sqrt{N}$, where N is the effective number of independent angular elastograms that are compounded. Angular compounding was performed in this paper by translating a phased-array transducer. A more efficient implementation of angular compounding would be to perform the acquisition of RF echo signals before and after compression, using a linear-array transducer with appropriate beam-steering angles, analogous to current compound B-mode imaging.

References

[1] J. Ophir, I. Cespedes, H. Ponnekanti, Y. Yazdi, and X. Li, "Elastography: A quantitative method for imaging the elasticity of biological tissues," *Ultrason. Imag.*, vol. 13, pp. 111–134, 1991.

[2] J. Ophir, S. K. Alam, B. Garra, F. Kallel, E. Konofagou, T. Krouskop, and T. Varghese, "Elastography: Ultrasonic estimation and imaging of the elastic properties of tissues," *Proc. Inst. Mech. Eng.*, vol. 213, pp. 203–233, 1999.

[3] T. Varghese, J. Ophir, E. Konofagou, F. Kallel, and R. Righetti, "Tradeoffs in elastographic imaging," *Ultrason. Imag.*, vol. 23, pp. 216–248, 2001.

[4] E. Cespedes, "Elastography: Imaging of biological tissue elasticity," Ph.D. dissertation, University of Houston, 1993.

[5] M. O'Donnell, A. R. Skovoroda, B. M. Shapo, and S. Y. Emelianov, "Internal displacement and strain imaging using ultrasonic speckle tracking," *IEEE Trans. Ultrason., Ferroelect., Freq. Contr.*, vol. 41, pp. 314–325, 1994.

[6] J. C. Bamber and N. L. Bush, "Freehand elasticity imaging using speckle decorrelation rate," *Acoust. Imaging*, vol. 22, pp. 285–292, 1996.

[7] K. J. Parker, S. R. Huang, R. A. Musulin, and R. M. Lerner, "Tissue response to mechanical vibrations for 'sonoelasticity imaging'," *Ultrasound Med. Biol.*, vol. 16, pp. 241–246, 1990.

[8] M. Bertrand, M. Meunier, M. Doucet, and G. Ferland, "Ultrasonic biomechanical strain gauge based on speckle tracking," in *Proc. IEEE Ultrason. Symp.*, 1989, pp. 859–864.

[9] T. A. Krouskop, D. R. Dougherty, and F. S. Vinson, "A pulsed Doppler ultrasonic system for making noninvasive measurements of the mechanical properties of soft tissue," *J. Rehabilitation Res. Dev.*, vol. 24, pp. 1–8, 1987.

[10] E. J. Chen, J. Novakofski, W. K. Jenkins, and W. D. O'Brien, Jr., "Young's modulus measurements of soft tissues with application to elasticity imaging," *IEEE Trans. Ultrason., Ferroelect., Freq. Contr.*, vol. 43, pp. 191–194, 1996.

[11] A. F. van der Steen, C. L. de Korte, and E. I. Cespedes, "Intravascular ultrasound elastography," *Ultraschall Med.*, vol. 19, pp. 196–201, 1998.

[12] M. F. Insana, L. T. Cook, M. Bilgen, P. Chaturvedi, and Y. Zhu, "Maximum-likelihood approach to strain imaging using ultrasound," *J. Acoust. Soc. Amer.*, vol. 107, pp. 1421–1434, 2000.

[13] R. Muthupillai, D. J. Lomas, P. J. Rossman, J. F. Greenleaf, A. Manduca, and R. L. Ehman, "Magnetic resonance elastography by direct visualization of propagating acoustic strain waves," *Science*, vol. 269, pp. 1854–1857, 1995.

[14] K. Nightingale, M. S. Soo, R. Nightingale, and G. Trahey, "Acoustic radiation force impulse imaging: In vivo demonstration of clinical feasibility," *Ultrasound Med. Biol.*, vol. 28, pp. 227–235, 2002.

[15] A. Pesavento, A. Lorenz, S. Siebers, and H. Ermert, "New realtime strain imaging concepts using diagnostic ultrasound," *Phys. Med. Biol.*, vol. 45, pp. 1423–1435, 2000.

[16] D. B. Plewes, J. Bishop, A. Samani, and J. Sciarretta, "Visualization and quantification of breast cancer biomechanical properties with magnetic resonance elastography," *Phys. Med. Biol.*, vol. 45, pp. 1591–1610, 2000.

[17] W. A. D. Anderson, *Pathology.* St. Louis, MO: C. V. Mosby, 1953.

[18] I. Cespedes and J. Ophir, "Reduction of image noise in elastography," *Ultrason. Imag.*, vol. 15, pp. 89–102, 1993.

[19] S. K. Alam and J. Ophir, "Reduction of signal decorrelation from mechanical compression of tissues by temporal stretching: Applications to elastography," *Ultrasound Med. Biol.*, vol. 23, pp. 95–105, 1997.

[20] S. K. Alam, J. Ophir, and E. E. Konofagou, "An adaptive strain estimator for elastography," *IEEE Trans. Ultrason., Ferroelect., Freq. Contr.*, vol. 45, pp. 461–472, 1998.
[21] T. Varghese, J. Ophir, and I. Cespedes, "Noise reduction in elastograms using temporal stretching with multicompression averaging," *Ultrasound Med. Biol.*, vol. 22, pp. 1043–1052, 1996.
[22] U. Techavipoo and T. Varghese, "Wavelet de-noising of displacement estimates in elastography," *Ultrasound Med. Biol.*, 2004, to be published.
[23] C. B. Burckhardt, "Speckle in ultrasound B-mode scans," *IEEE Trans. Sonics Ultrason.*, vol. 25, pp. 1–6, 1978.
[24] H. Ping, "Spatial compounding in 3D imaging of limbs," *Ultrason. Imag.*, vol. 19, pp. 251–265, 1997.
[25] M. O'Donnell and S. D. Silverstein, "Optimum displacement for compound image generation in medical ultrasound," *IEEE Trans. Ultrason., Ferroelect., Freq. Contr.*, vol. 35, pp. 470–476, 1988.
[26] M. Tanter, J. Bercoff, L. Sandrin, and M. Fink, "Ultrafast compound imaging for 2-D motion vector estimation: Application to transient elastography," *IEEE Trans. Ultrason., Ferroelect., Freq. Contr.*, vol. 49, pp. 1363–1374, 2002.
[27] G. E. Trahey, S. W. Smith, and O. T. von-Ramm, "Speckle pattern correlation with lateral aperture translation: Experimental results and implications for spatial compounding," *IEEE Trans. Ultrason., Ferroelect., Freq. Contr.*, vol. 33, pp. 257–264, 1986.
[28] R. F. Wagner, M. F. Insana, and S. W. Smith, "Fundamental correlation lengths of coherent speckle in medical ultrasonic images," *IEEE Trans. Ultrason., Ferroelect., Freq. Contr.*, vol. 35, pp. 34–44, 1988.
[29] R. R. Entrekin, B. A. Porter, H. H. Sillesen, A. D. Wong, P. L. Cooperberg, and C. H. Fix, "Real-time spatial compound imaging: Application to breast, vascular, and musculoskeletal ultrasound," *Semin Ultrasound CT MR*, vol. 22, pp. 50–64, 2001.
[30] F. Kallel and J. Ophir, "A least-squares strain estimator for elastography," *Ultrason. Imag.*, vol. 19, pp. 195–208, 1997.
[31] E. L. Madsen, G. R. Frank, T. A. Krouskop, T. Varghese, F. Kallel, and J. Ophir, "Tissue-mimicking oil-in-gelatin emulsions for use in heterogeneous elastography phantoms," *Ultrason. Imag.*, vol. 25, pp. 17–38, 2003.
[32] A. P. Berkhoff, H. J. Huisman, J. M. Thijssen, E. M. Jacobs, and R. J. Homan, "Fast scan conversion algorithms for displaying ultrasound sector images," *Ultrason. Imag.*, vol. 16, pp. 87–108, 1994.
[33] W. D. Richard and R. M. Arthur, "Real-time ultrasonic scan conversion via linear interpolation of oversampled vectors," *Ultrason. Imag.*, vol. 16, pp. 109–123, 1994.
[34] T. Varghese and J. Ophir, "A theoretical framework for performance characterization of elastography: The strain filter," *IEEE Trans. Ultrason., Ferroelect., Freq. Contr.*, vol. 44, pp. 164–172, 1997.
[35] S. Srinivasan, R. Righetti, and J. Ophir, "Trade-offs between the axial resolution and the signal-to-noise ratio in elastography," *Ultrasound Med. Biol.*, vol. 29, pp. 847–866, 2003.
[36] R. Righetti, J. Ophir, and P. Ktonas, "Axial resolution in elastography," *Ultrasound Med. Biol.*, vol. 28, pp. 101–113, 2002.
[37] A. P. Sarvazyan, "Low-frequency acoustic characteristics of biological tissues," *Polym. Mech.*, vol. 11, pp. 594–597, 1975.
[38] A. R. Skovoroda, S. Y. Emelianov, and M. O'Donnell, "Tissue elasticity reconstruction based on ultrasonic displacement and strain images," *IEEE Trans. Ultrason., Ferroelect., Freq. Contr.*, vol. 42, pp. 747–765, 1995.

Udomchai Techavipoo (S'01) was born in Bangkok, Thailand, on September 16, 1973. He received the B.Eng.E.E. degree from Kasetsart University, Bangkok, Thailand, in 1994. In 1997, he received a scholarship from Anandamahidol Foundation, Thailand, to pursue graduate studies at the College of Engineering, University of Michigan, Ann Arbor, and received the M.S.E.E. degree in 1999.

He is currently pursuing a Ph.D, degree in electrical and computer engineering, University of Wisconsin (UW), Madison. He is a graduate student research assistant at the UW Ultrasound Laboratory, Department of Medical Physics, and working on ultrasound elastography, non-invasive temperature estimation and image segmentation. His research interests include wavelet applications, detection and estimation theory, and image and signal processing in medical imaging.

Quan Chen (S'03) was born in Xinhua, China, in 1975. He received his B.S. degree in physics from Nanjing University, Nanjing, China, in 1996. He spent 2 years in the master's program in physics, Southeast University, Nanjing, China, before coming to the United States in 1998. He earned a M.S. degree in medical physics in 2000 and is pursuing the Ph.D. degree in medical physics at the University of Wisconsin-Madison.

His research interests include contrast agent simulation, bubble dynamics, elastography, ultrasound image segmentation, and computer modeling in ultrasound.

Tomy Varghese (S'92–M'95–SM'00) received the B.E. degree in instrumentation technology from the University of Mysore, Mysore, India, in 1988, and the M.S. and Ph.D. degrees in electrical engineering from the University of Kentucky, Lexington, KY, in 1992 and 1995, respectively. From 1988 to 1990 he was employed as an engineer in Wipro Information Technology Ltd., Mysore, India. From 1995 to 2000, he was a postdoctoral research associate at the Ultrasonics Laboratory, Department of Radiology, University of Texas Medical School, Houston. He is currently an assistant professor in the Department of Medical Physics and Biomedical Engineering at the University of Wisconsin-Madison.

His current research interests include elastography, ultrasound imaging, ultrasonic tissue characterization, detection and estimation theory, statistical pattern recognition, and signal and image processing applications in medical imaging. Dr. Varghese is a member of the IEEE, the American Institute of Ultrasound in Medicine (AIUM), the American Association of Physicists in Medicine (AAPM), and Eta Kappa Nu.

James A. Zagzebski (A'89) was born in Steven Points, WI, in 1944. He received the B.S. degree in physics from St. Mary's College, Winona, MN, in 1966, and the M.S. degree in physics in 1968 and the Ph.D. degree in radiological sciences in 1972 from the University of Wisconsin, Madison. He is a Professor of medical physics and of radiology and human oncology at the University of Wisconsin.

His research interests include ultrasound imaging and tissue characterization, flow detection and visualization using ultrasound, and technological assessment of imaging devices. Dr. Zagzebski's professional affiliations include the IEEE, the American Institute of Ultrasound in Medicine, and the American Association of Physicists in Medicine.

Ernest L. Madsen received his B.S. and M.S. degrees in physics at the University of Maryland-College Park, and his Ph.D. degree in physics at the Catholic University of America, Washington, DC, in 1968. He has worked in medical ultrasound and magnetic resonance imaging phantoms for the past 27 years.

Dr. Madsen was Professor of Medical Physics at the University of Wisconsin-Madison until July 2002 when he officially retired. However, he continues as Professor Emeritus working on phantom development, particularly for use in ultrasound and MR elastography. He is a Fellow of the American Institute of Ultrasound in Medicine and of the American Association of Physicists in Medicine.